Sensors and Actuators A 315 (2020) 112221

Contents lists available at ScienceDirect

Sensors and Actuators A: Physical

journal homepage: www.elsevier.com/locate/sna

Compliant underwater manipulator with integrated tactile sensor for nonlinear force feedback control of an SMA actuation system

Maohua Lin [a], Morteza Vatani [b], Jae-Won Choi [b], Savas Dilibal [c], Erik D. Engeberg [a,*]

[a] Department of Ocean and Mechanical Engineering, Florida Atlantic University, Boca Raton, FL 33431, USA
[b] University of Akron, Mechanical Engineering Department, Akron, OH, 44325, USA
[c] Mechatronics Engineering Department, Istanbul Gedik University, Yakacık Kartal, Istanbul, 34876 ,Turkey

ARTICLE INFO

Article history:
Received 21 April 2020
Received in revised form 2 July 2020
Accepted 21 July 2020
Available online 10 August 2020

Keywords:
Soft robot
Tactile sensor
Multi-physics simulation
Shape memory alloy
Electromyogram

ABSTRACT

Design, sensing, and control of underwater gripping systems remain challenges for soft robotic manipulators. Our study investigates these critical issues by designing a shape memory alloy (SMA) actuation system for a soft robotic finger with a directly 3D-printed stretchable skin-like tactile sensor. SMA actuators were thermomechanically trained to assume a curved finger-like shape when Joule heated, and the flexible multi-layered tactile sensor was directly 3D-printed onto the surface of the fingertip. A nonlinear controller was developed to enable precise fingertip force control using feedback from the compliant tactile sensor. Underwater experiments were conducted using closed-loop force feedback from the directly 3D-printed tactile sensor with the SMA actuators, showing satisfactory force tracking ability. Furthermore, a 3D finite element model was developed to more deeply understand the shape memory thermal-fluidic-structural multi-physics simulation of the manipulator underwater. An application for human control via electromyogram (EMG) signals also demonstrated an intuitive way for a person to operate the submerged robotic finger. Together, these results suggested that the soft robotic finger could be used to carefully manipulate fragile objects underwater.

1. Introduction

The ocean is full of biological and mineral resources. However, studying and exploring these resources from the ocean remains a challenge, which is why underwater manipulators with embedded tactile sensors have been recently developed as an essential tool to use in murky and turbid environments [1–3]. Tactile sensors provide real-time feedback of the manipulator to accurately adjust the grip force underwater and to detect contact with different objects [4–6]. Previous studies have advanced the design and development of flexible and integrated tactile sensors [7–10]. Although these sensors have shown potential in providing precise and repeatable information, there is still a need for compliant and stretchable tactile sensors that are suitable to integrate within a soft robotic manipulator for underwater use [11–13]. Additionally, the use of tactile sensors is required to be highly reliable even in corrosive underwater environments—only a few sensors have been reported with underwater sensing capability and the underwater versatility is limited with current technologies [14–16]. Furthermore, the fabrication cost for the sensing systems could be high due to complex wiring topology, packaging and tough assembly [17,18].

Recently, highly stretchable tactile sensors were developed using ionic conductive polymer composites as a piezoresistive material and a CNT-based nanocomposite as the electrode materials [19,20]. CNTs in a polymer matrix generate conducting networks, while the polymer matrix provides easy manufacturability [21,22]. Additionally, CNTs have also been widely used as a sensing material because of their superior mechanical and electrical properties [22,23]. Examples include a piezoresistive strain sensor [24], conductors used in polymer MEMS [25], and also a microstrain polymer/CNT sensor [26]. Compared to these examples with rigid sensors, there are several reports on stretchable piezoresistive sensors and electronics with stretchable rubberlike conductors [27], CNT/polymer strain sensors [28], and silver/CNT conductive rubber adhesives [29,30]. Furthermore, the single-walled carbon nanotube strain sensor showed superior water resiliency, which indicated that the sensor could be used for underwater robotic safety management [14].

For these reasons, a multi-layered tactile sensor was developed and directly 3D-printed on the inner assembly of a robotic fingertip antagonistically actuated by two SMA plates in this paper (Fig. 1).

* Corresponding author.
E-mail address: eengeberg@fau.edu (E.D. Engeberg).

https://doi.org/10.1016/j.sna.2020.112221
0924-4247/

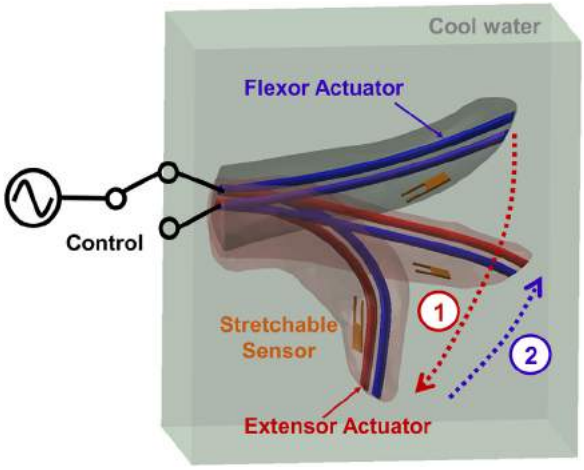

Fig. 1. Antagonistic actuation concept using two thermomechanically trained SMA plates. Integrated tactile sensing enables force control. The color of the actuators indicates the temperature during different times in the actuation cycle, where Joule heating is used to alternately flex and extend the actuators to drive the finger.

The new multi-layered tactile sensor was composed of three main components: an intermediate piezoresistive polymer to detect the sensory information, conductive, and flexible polymer electrodes to transfer the sensory information and an insulator polymer to shield the components. Incorporation of carbon nanotubes (CNTs) into a polymer matrix to make conductive nanocomposites were reported as a flexible method for creating conductive as well as sensing elements.

Previously, the authors have demonstrated position control of a novel anthropomorphic robotic finger with human-inspired SMA actuators that were thermomechanically trained to bend at locations similar to the three joints of a human finger [31]. New in this paper, a multi-layered polymeric skin-like tactile sensor was directly 3D-printed onto the anthropomorphic robotic fingertip, which housed two antagonistic SMA actuators that were trained to make curved and straight shapes (Fig. 1). Through the newly developed nonlinear force control system, the precise fingertip force tracking was enabled using feedback from the compliant, multi-layered tactile sensor. To understand the behavior of the complex submerged manipulator under nonlinear force control, a 3D finite element model was developed to verify and explain the shape memory thermal-fluidic-structural multi-physics behavior of the SMA actuators underwater. To the best knowledge of the authors, electromyogram (EMG) was used for the first time for the tele-operated control of an underwater robotic manipulator [32]. Therefore, the new robotic finger for underwater applications has the potential for precise fingertip force control and could facilitate the collection of samples and characterization of resources in the ocean.

The prime goal of this study was to investigate and understand the potential for force control using feedback from the multi-layered polymeric skin-like tactile sensor with the underwater manipulator. The fabrication process for the multi-layered force sensor and manipulator was explained. The nonlinear force controller for the finger was evaluated with steps, sinusoids, and EMG input signals using feedback from the tactile sensor. The thermal-fluidic-structural performance of the nonlinear SMA actuation system was verified and explained by finite element analysis.

2. Materials and methods

Two antagonistically actuated SMA plate actuators were arranged in parallel within the robotic finger, which were cooled using water from the underwater environment (Fig. 1). The flexor actuator was thermomechanically trained to take a curved shape when Joule heated, whereas the extensor actuator took a straight shape when Joule heated. These two SMA actuators were placed in parallel and housed within an inner finger assembly. With this design, alternating between heating and cooling the flexor and extensor actuators caused the finger to flex and extend. A multi-layered tactile sensor was directly 3D-printed on the inner assembly of the fingertip, and also, a nonlinear force controller was designed to control the force of the finger accurately.

2.1. Materials

Polycrystalline NiTi SMA plates with a thickness of 1 mm were purchased from Memry (Weil am Rhein, Germany). The NiTi SMA had a Ni50.1Ti49.9 atomic weight composition. Each NiTi SMA actuator was cut from a plate into the shape of a 'U' using an electric discharge machine (Fig. 2d(iii)). The initial thermomechanical training dictates the full recovery of the antagonistic actuators. At least 100 thermal cycles are required for repeatable antagonistic bending actuation. Particularly, the cyclic actuation stroke tends to stabilize through thermal cycling during three remarkable stabilizing stages: the early-evolution, transient, and stabilization stages [33].

FullCure® 930 TangoPlus, a 3D printing photopolymer from Stratasys Inc (Eden Prairie, MN, USA), was used as the primary matrix of the conductive electrodes. CN9021 was a highly flexible photocurable monofunctional monomer from Sartomer America used to develop the piezoresistive pressure-sensitive polymer. Pol-Ease® 2450 from Polytek Development (Williams Township, PA, USA) acted as a releasing agent used in a molding process and PT Flex 20 Liquid Rubber (Shore A20) was used due to its fast cure time (~5 min). Multi-walled carbon nanotubes (MWNTs, ≥85 %) with a diameter of 10–30 nm and length of 5–20 μm were purchased from Nano Lab (Waltham, MA, USA). Triton™ X100 was used as a surfactant, N, N-dimethylformamide (DMF, ≥99.9 %) was used as a solvent, 1-ethyl-3-methylimidazolium tetrafluoroborate (EMIBF4) was the ionic liquid (IL), and 2,2-dimethoxy-2-phenylacetophonene (DMPA) was used as a photoinitiator (Sigma-Aldrich, Milwaukee, USA). TRIGONOX 12C75, a thermal initiator, was purchased from Akzo Nobel Functional Chemicals AB (Chicago, USA).

Conductive electrodes were developed by dispersion of non-covalently functionalized MWNTs into a photo and thermal-curable photopolymer. The amount of MWNTs was selected to be above the percolation conductive network [31,34]. First, 5 wt% of MWNTs were non-covalently functionalized through their dispersion into a solution of Triton X100 and DMF with a ratio of 1:350. This solution was blended using a sonicator (Q700, Qsonica, Newtown, CT, USA) for 20 min under the pulse mode (60 s on and 10 s off). After functionalization, the TangoPlus was added to the solution to generate a 5 wt% nanocomposite solution. This mixture was stirred on a hot plate magnetic stirrer at 80 °C and 400 RPM for 48 h to evaporate the solvent. Finally, 4 wt% of TRIGONOX 125C75 was added to the mixture and blended using a high-speed mixer (DAC 150.1 FVZ-K, FlackTek Inc. Landrum, SC, USA) at 2500 RPM for 5 min. The pressure-sensitive composite was prepared by blending EMIBF4 and CN9021 using the high-speed mixer also at 2500 RPM for 5 min. 2 wt% DMPA was also added to the mixture using a magnetic stirrer to generate reactive species during exposure to 365 nm UV light and to facilitate the photopolymerization.

2.2. Fabrication of anthropomorphic finger

The whole finger manipulator schematic consists of three main parts: SMA plates, multilayered tactile sensors, and electrical insu-

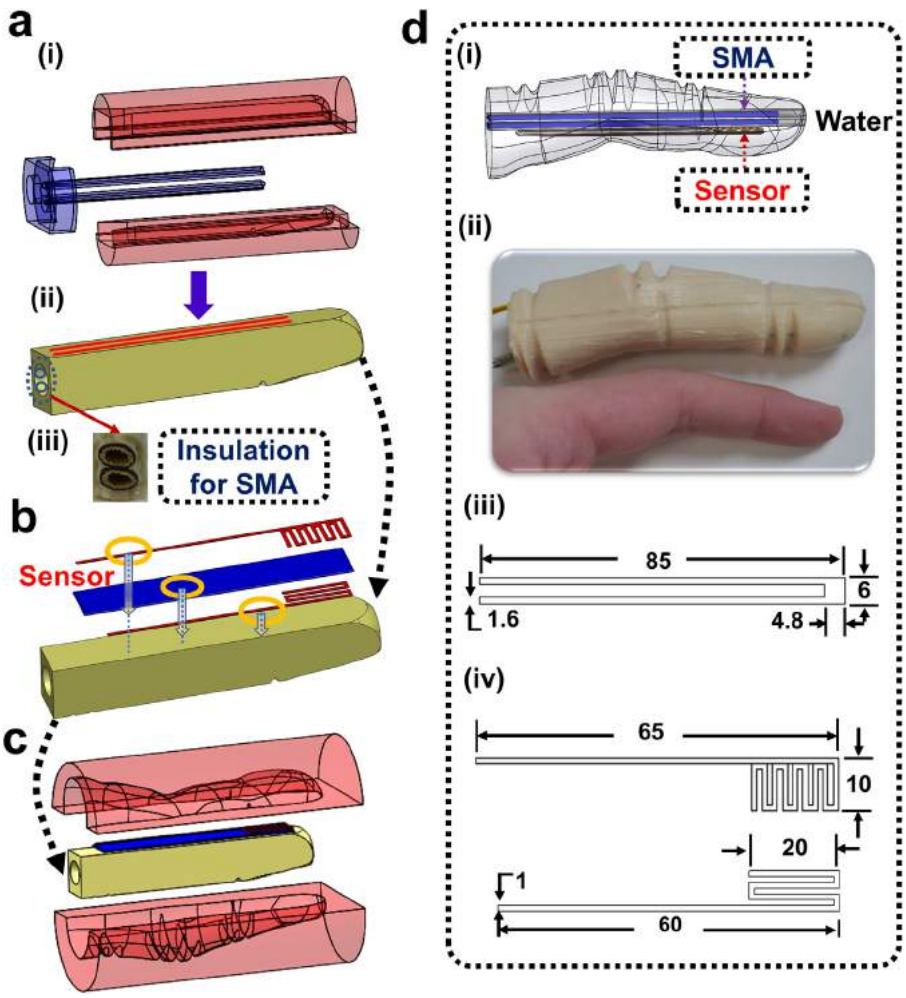

Fig. 2. a. (i) Fabrication of the first mold to create the inner part of the finger: exploded and assembled view for SMA, (ii) Inner finger assembly after molding, (iii) Thermal/electrical insulator tubes for the SMA plates. b. 3D printing a tactile sensor on the inner molded part. c. Placing the inner mold part in the outer mold. d. (i) Assembled underwater manipulator schematic, (ii) The final assembled manipulator compared with human finger, (iii) Top view of each 'U' shaped SMA actuator that was cut from a 1 mm thick plate using an electric discharge machine, (iv) Top view of tactile sensor's upper and lower layers (unit: mm).

lators (Fig. 2). Two main molds and one 3D printing step were created to make the whole manipulator (Fig. 2a–c). In the first mold (Fig. 2a(i)), there were two parts; the outer part was for creating the finger shape, and the inner part was to house the SMA actuators with the sensor 3D-printed on the outer surface of the inner part. An outer mold was created from a 3D human finger model, which was 3D printed (Cube X Trio, 3D Systems, Rock Hill, USA) with polylactic acid (PLA) material.

Pol-Ease® 2450 was applied to the 3D printed molds for easy release. The two components of the PT Flex 20 were mixed with a 1:1 ratio using the high-speed shear mixer, which also helped to remove air bubbles trapped in the mixture during handling. Because each SMA actuator was to be Joule heated, two thermal/electrical insulator tubes were embedded within the inner mold (Fig. 2a(ii–iii)) using T117EA4B thermal insulation tubing with an American Wire Gauge of 4 (Delfingen, Rochester Hills, USA). These insulators surrounded the SMA actuators and prevented the finger skin material from melting when the SMA actuators were heated and also electrically isolated the actuators from each other. Additionally, the insulating tubes were left open at the base and tip to enable water to flow through and cool the actuators as the finger was flexed and extended underwater.

After placing the insulating tubes into the inner finger assembly, the prepared rubber material was cast at room temperature. The inner part was ready to remove from the mold after 90 min. Then, the flexible tactile sensor was 3D printed on the molded part (Fig. 2b), described in the following section, to provide feedback for the nonlinear fingertip force controller. The molded inner part (Fig. 2c) was next placed in the outer mold to produce the final finger part with the integrated tactile sensor for detecting fingertip forces.

2.3. Tactile sensor fabrication

A pressure-sensitive taxel was fabricated using a hybrid additive manufacturing process, including repeated molding and direct printing [35]. As shown in Fig. 2b, the fabricated taxel consisted of three main components; a casted pressure-sensitive polymer (blue in Fig. 2b) sandwiched between two layers of directly 3D-printed stretchable electrode strips (red in Fig. 2b).

Using the developed three-axis direct-print photopolymerization machine [31,34], the parameters (speed, flow-rate, and nozzle size) were adjusted to print electrode materials with 1 mm width and the pattern shown in Fig. 2d(iv)). This taxel acted like a mechanoreceptor in the skin, that was formed with the crossing electrodes and the sensing composite, which could be potentially extended to any size (20 mm x 10 mm in this paper, Fig. 2 d(iii–iv)) or as many taxels as desired by having additional crossing electrodes [36]. By incorporating this sensor into a Wheatstone bridge, it was possible to correlate the voltage change to an externally

applied force that deforms the sensor. After fabrication of the sensor and connecting the electrical wires, it was then fully embedded into the finger body by the final casting of the soft urethane material, as shown in Fig. 2c to form the finger (Fig. 2d(i–ii)).

2.4. Nonlinear force controller architecture

A nonlinear force controller was developed using an outer feedback loop to create a force error signal along with two inner current control loops using MOSFETs to Joule heat the flexor and extensor actuators (Fig. 3). The outer force control loop was based on the error:

$$e = F_D - F \tag{1}$$

defined as the difference between the desired force (F_D) and the force (F) measured by the directly printed tactile sensor.

Next, an error manifold was formulated as:

$$S = K_P e + K_I \int e dt + K_D \dot{e} \tag{2}$$

where K_P, K_I, and K_D are the proportional, integral, and derivative gains, respectively. S was saturated at maximum permissible levels ($\pm\sigma$) to enable high gains and aggressive minimization of force tracking error. By design, heating the flexor actuator minimized positive force errors whereas heating the extensor minimized negative force tracking errors because the actuators apply forces in opposing directions (Fig. 1). Hence, the control laws for each SMA actuator were never simultaneously active. The control laws for the flexor and extensor actuators, δ_F and δ_E, respectively are:

$$\delta_F = \sigma_F sat(S), \sigma_F = \frac{\sigma,\ S > 0}{0,\ S \leq 0} \tag{3}$$

$$\delta_E = \sigma_E sat(S),\ \sigma_E = \frac{\sigma,\ S < 0}{0,\ S \geq 0} \tag{4}$$

The positive values of manifold S were passed into the inner current control loop for Joule heating the flexor SMA actuator (SMA_F). The current passing through the flexor actuator (I_F) was measured with an ACS712 Hall effect sensor (Allegro MicroSystems) and was used as feedback to control the current flow [31]. Thus, Joule heating the flexor actuator caused the finger to flex and increase the applied force. Conversely, the negative portion of the manifold S was passed through an absolute value function to become positive once again and enter another identical MOSFET current control loop to heat the extensor SMA actuator (SMA_E). Accordingly, the current passing through the extensor actuator (I_E) was controlled using feedback from another ACS712 Hall effect sensor. These two control signals for Joule heating the flexor and extensor were mutually exclusive so that heating the flexor actuator caused the finger to increase the force while heating the extensor actuator caused the finger to reduce the applied force and extend.

The nonlinear controller for the robotic finger was implemented in MATLAB/Simulink (The MathWorks) using the real-time windows target kernel and a PCI-6221 card interfaced with a BNC 2090 connector block (National Instruments). The Hall effect and tactile sensor signal sample rates were 1 kHz, as was the control loop update rate.

2.5. Experimental methods for nonlinear force control

The novel SMA-actuated robotic finger was mounted underwater within an aquarium (Fig. 7a). A pencil was also mounted within the workspace of the finger to provide an appropriately sized object upon which the finger could apply forces controlled by feedback from the directly 3D-printed tactile sensor.

Step input tracking experiments were performed with seven different amplitudes of desired force (F_D) ranging from 0.77 N to 9.33 N. Four cycles of each step input amplitude were observed to determine the ability to track a step input and to verify the ability to control a range of fingertip forces. This range of forces was selected to investigate the ability to precisely control relatively small fingertip forces to demonstrate the potential to delicately and accurately grasp fragile objects. The highest force of 9.33 N was selected to be well within the SMA material capabilities without causing any plastic deformation.

Next, the finger was excited by sinusoidal desired force inputs with high and low amplitudes of 6 N and 3 N, respectively. Five different frequencies of sinusoidal inputs were explored with both high and low desired force inputs: 0.15, 0.3, 0.45, 0.6, and 0.75 rad/s. This produced ten experimental conditions with sinusoidal tracking experiments. The absolute mean error was calculated for the sine tracking experiments to quantify the performance of the nonlinear force controller. A two-factor analysis of variance (ANOVA) was performed to determine if the amplitude or frequency significantly impacted the absolute mean error.

2.6. Application for EMG control of the robotic finger

To demonstrate an application of the finger to be controlled by a person, electromyogram (EMG) was used as an input, which is the first time EMG has been used to control an underwater manipulator, to the best knowledge of the authors. EMG is a voltage related to the level of muscle contraction and is commonly used to control prosthetic hands and in other tele-operated robotic applications [37,38]. In this paper, MyoLab II (Motion Control, Salt Lake City, USA) was used to record, filter, rectify, and amplify the EMG signals from the forearm of a person. EMG was recorded from two sites on the posterior and anterior compartments of the forearm. The difference between these two signals functioned as the desired force input for the nonlinear force controller. In this intuitive manner, a person could flex his or her wrist to cause the finger to flex and increase the applied fingertip force. Conversely, extending the wrist would cause the finger to extend and decrease the applied fingertip force. This straightforward method of interpreting the human intention to control the manipulator was demonstrated as an application for tele-operated control of the submerged robotic finger.

2.7. Finite element modeling methods

The shape memory behavior of SMA was captured by a 3D constitutive model proposed by Auricchio in the built-in library of COMSOL Multiphysics software [31,39–42]. Table 1 summarizes the material properties of SMA NiTi alloy [31,39,40]. The behavior of the U-shaped SMA actuators was trained under displacement and then was heated from 28 °C to 72 °C in step 1 (from 0–1 s). Then the SMA was cooled until 1.5 s.

In the experimental studies, we focused on the effects of different frequencies and different loads on the thermal-fluidic-structural fields of the underwater manipulator. Therefore, it is important to develop a model to predict the fluid, temperature and displacement distributions and more deeply understand the functionality of this complex system. The built-in COMSOL heat transfer, fluid flow and structural mechanics module were used and coupled together to simulate the Multiphysics phenomena of the underwater manipulator. The targeted object upon which the finger exerted force was consistently assumed to be 3 cm away from the fingertip. The Joule heating was quick, so the boundary and domain temperatures of the SMA were assumed as 72 °C when the SMA was heated. The internal water within the insulated cavities surrounding each SMA actuator and the boundary of the SMA was assumed as 28 °C.

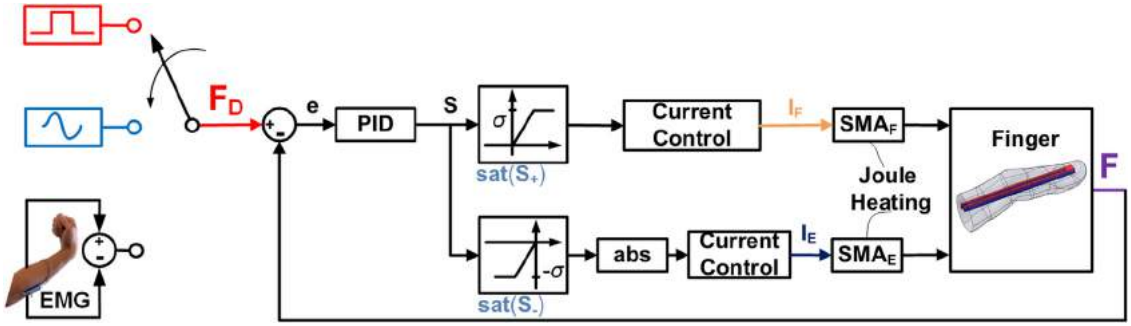

Fig. 3. Nonlinear force controller for the finger using feedback from the directly printed tactile sensor. This was evaluated with three different kinds of inputs: steps, sinusoids, and EMG signals.

Table 1
Mechanical and thermal properties used in comsol model.

Property	Unit	Value
SMA elastic modulus of austenite	GPa	51.7
SMA elastic modulus of martensite	GPa	42
SMA poisson's ratio	N/A	0.3
SMA hardening parameter, H	MPa	85
SMA elastic limit, R	MPa	192
SMA temperature scaling parameter	MPa/°C	2
SMA maximum strain	mm/mm	0.04
SMA thermal conductivity	W/(m · °C)	18
SMA average heat capacity	J/ kg · °C	320
SMA martensite start temperature	°C	28.6
SMA martensite finish temperature	°C	48.8
SMA austenite start temperature	°C	51.5
SMA austenite finish temperature	°C	70.6
Viscosity of water	Pa · s	8.90×10^{-4}
c_{10}	MPa	0.4
c_{01}	MPa	0.1
Rubber density	kg/m^3	1522
SMA density	kg/m^3	6450
Water density	kg/m^3	1000

To further understand the thermal-fluidic-structural mechanisms of the underwater manipulator under different frequencies and different loads, a computational simulation was used to observe the distributions of the fluid, pressure, thermal and structural displacement under three different conditions: (i) 0.45 rad/s with low (F_L) amplitude sinusoidal desired force input of 3 N; (ii) 0.45 rad/s with high (F_H) amplitude desired force input of 6 N; (iii) 0.75 rad/s with high (F_H) amplitude desired force input of 6 N. These correspond to several key conditions used during the sinusoidal tracking experiments.

The flow of the underwater system was assumed to be laminar Newtonian, viscous and incompressible. The Navier-Stokes equations in Lagrangian-Eulerian formulation were used as the governing equations [43–45]:

$$\frac{\partial \rho_f}{\partial t} + \nabla \cdot (\rho_f \boldsymbol{u}) = 0 \tag{5}$$

$$\frac{\partial (\rho_f \boldsymbol{u})}{\partial t} + \rho_f (\boldsymbol{u} - \boldsymbol{u_m}) \nabla) \cdot \boldsymbol{u} - \mu (\nabla (\left(\nabla \boldsymbol{u} + (\nabla \boldsymbol{u})^T \right) + \nabla \cdot p - \rho_0 g \beta_T (T - T_0) = 0 \tag{6}$$

where t is the time, ρ_f is the fluid's density, $\boldsymbol{u}$ is the velocity vector, $\boldsymbol{u}_m$ is the mesh velocity due to the movement of the coordinate system, μ is the viscosity of the fluid, p is the fluid pressure, ρ_0 is the reference density, g is the gravitational acceleration vector, β_T is the thermal expansion coefficient of the fluid, T is the temperature, T_0 is the reference temperature, and ∇ is the differential operator with respect to the Eulerian coordinate. The heat transfer in the entire manipulator system is described as [43]:

$$\frac{\partial (\rho_i C_{p,i} T)}{\partial t} + \nabla \cdot \left(\rho_i C_{p,i} T \boldsymbol{u} \right) = \nabla \cdot (k_i \nabla T) \tag{7}$$

where the subscript i indicates SMA and water, k_i and $C_{p,i}$ represent the thermal conductivity and specific heat of material at the ith domain, respectively.

The structural deformations of the rubber finger and tactile sensor materials were solved using a two-parameter incompressible Mooney-Rivlin material model [46]. The governing equation [44,45] for the solid can be described by the following equation:

$$\nabla \boldsymbol{\sigma} + \boldsymbol{F}_s = \rho_s \frac{\partial^2 d_s}{\partial t^2} \tag{8}$$

$$P = 2(1 - \lambda^{-3})(\lambda c_{10} + c_{01}) \tag{9}$$

where ρ_s is the solid density, $\boldsymbol{\sigma}$ is the Cauchy stress tensor, $\boldsymbol{F}_s$ is the body force per unit volume, d_s is the displacement of the solid, P is the first Piola-Kirchhoff stress tensor, c_{10} and c_{01} are Mooney-Rivlin material parameters, and λ is the value of the principal stretches. The wall between the solid and fluid experienced a load from the fluid, given by [44]:

$$\boldsymbol{F}_T = -\boldsymbol{n} \left(-p\boldsymbol{I} + \mu \left(\nabla \boldsymbol{u} + (\nabla \boldsymbol{u})^T \right) \right) \tag{10}$$

where $\boldsymbol{n}$ is the normal vector to the boundary, and $\boldsymbol{I}$ is the identity tensor. This load represents a sum of pressure and viscous forces. The wall was assumed to be isotropic, linear, and nearly incompressible. A uniform flow was assigned at the inlet and a pressure boundary was assigned at the outlet. For the solid structural components, the boundary conditions included fixed displacements at the inlet, and free displacement of the wall. The targeted object upon which the finger applied force was assumed to be rigid and fixed.

3. Results

3.1. Step input force tracking

Illustrative data from the step responses with an amplitude of 7.78 N showed satisfactory force tracking ability, where each cycle ran for 10 s (Fig. 4(a)). At the beginning of each step, the error increased sharply as expected (Fig. 4(b)), but this was rapidly minimized due to the action of the nonlinear force feedback controller, which saturated at the maximum positive and negative permissible levels to aggressively minimize the error (Fig. 4(c)). The electrical current flow measured through each SMA actuator showed cyclical patters on the rising and falling edges of each step: the flexor actuator current (I_F) increased to apply and maintain fingertip forces whereas the extensor actuator current flow (I_E) increased

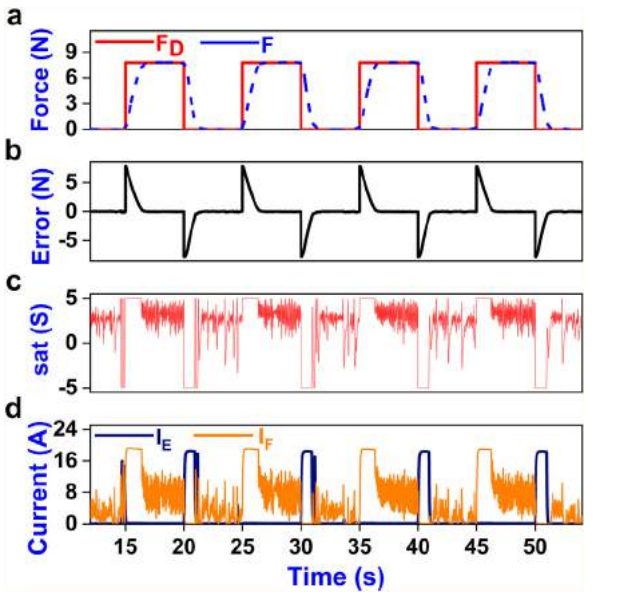

Fig. 4. Illustrative data of the step response of the finger. a. The 7.78 N amplitude input was accurately tracked. b. The error of the system increased sharply at the rising edge of each step input but was rapidly driven to zero. c. The manifold (S) of the nonlinear force controller saturated at the maximum and minimum permissible levels to rapidly minimize the force tracking error. d. Current flowed through the flexor SMA actuator (I_F) to increase and maintain the applied fingertip force whereas current flowed through the extensor actuator (I_E) to decrease the fingertip force.

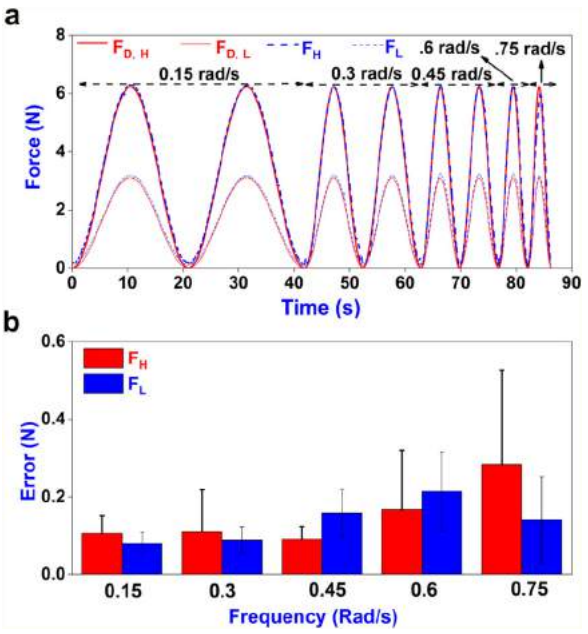

Fig. 6. a. Illustrative sinusoidal tracking data for the high and low amplitudes with five different frequencies. b. Means and standard deviations of the sinusoidal tracking experiments with the high (F_H) and low (F_L) amplitude desired force inputs of 6 N and 3 N, respectively.

to reduce the applied fingertip force (Fig. 4(d)). The peak current flow was saturated at 19.4A. Because the MOSFET voltage supply was a constant 5 V, the peak power consumption was nearly 100 W.

A consistent pattern emerged with each cycle of force application during the step responses that were evaluated with seven different amplitudes: 0.77, 1.55, 3.11, 4.66, 6.22, 7.78 and 9.33 N (Fig. 5). The robotic finger stably controlled fingertip forces over the entire range from 0.77 N to 9.33 N with no overshoot observed at any step amplitude and steady-state error was consistently minimal. A superposition of the seven step amplitudes revealed a consistent SMA force control profile with slopes that were almost identical on the increasing and decreasing portions of the force trajectory tracking (Fig. 5(b)). The control process was recorded and shown in supplemental 2.

3.2. Sinusoidal input force tracking

The sinusoidal force tracking ability of the fingertip force controller with high and low force amplitudes over the range of frequencies from $\omega = 0.15$, 0.3, 0.45, 0.6, and 0.75 rad/s demonstrated satisfactory error tracking abilities (Fig. 6(a)). The mean and standard deviations of the sinusoidal tracking experiments with the high (F_H) and low (F_L) amplitude desired force inputs of 6 N and 3 N, respectively showed that all mean average error values were under 0.3 N. Averaged across all frequencies of actuation, for the low amplitude sinewave of 3 N, the mean and standard deviation error was 0.14 ± 0.067 N (Fig. 6(b)). For the high amplitude sinewave of 6 N, the overall mean and standard deviation of the force error was 0.15 ± 0.12 N. Thus, the mean errors as a percentage of the input amplitude were 4.6 % and 2.5 % for the low and high amplitude forces, respectively. The two-factor ANOVA indicated that neither the amplitude nor the frequency significantly

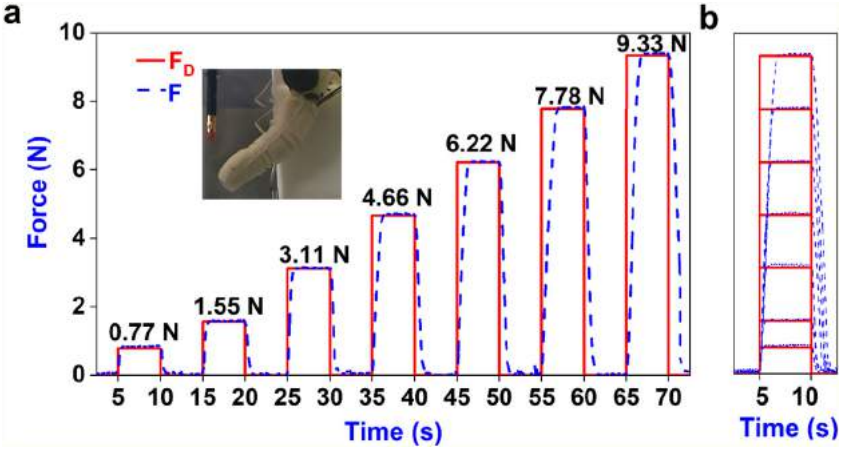

Fig. 5. a. Step responses of the SMA actuated finger with force feedback from the directly 3D-printed compliant tactile sensor. Force tracking and steady state error were satisfactory for all amplitudes. b. The slope of the increasing and decreasing forces were nearly identical for all step amplitudes, as demonstrated by the superposition of the data.

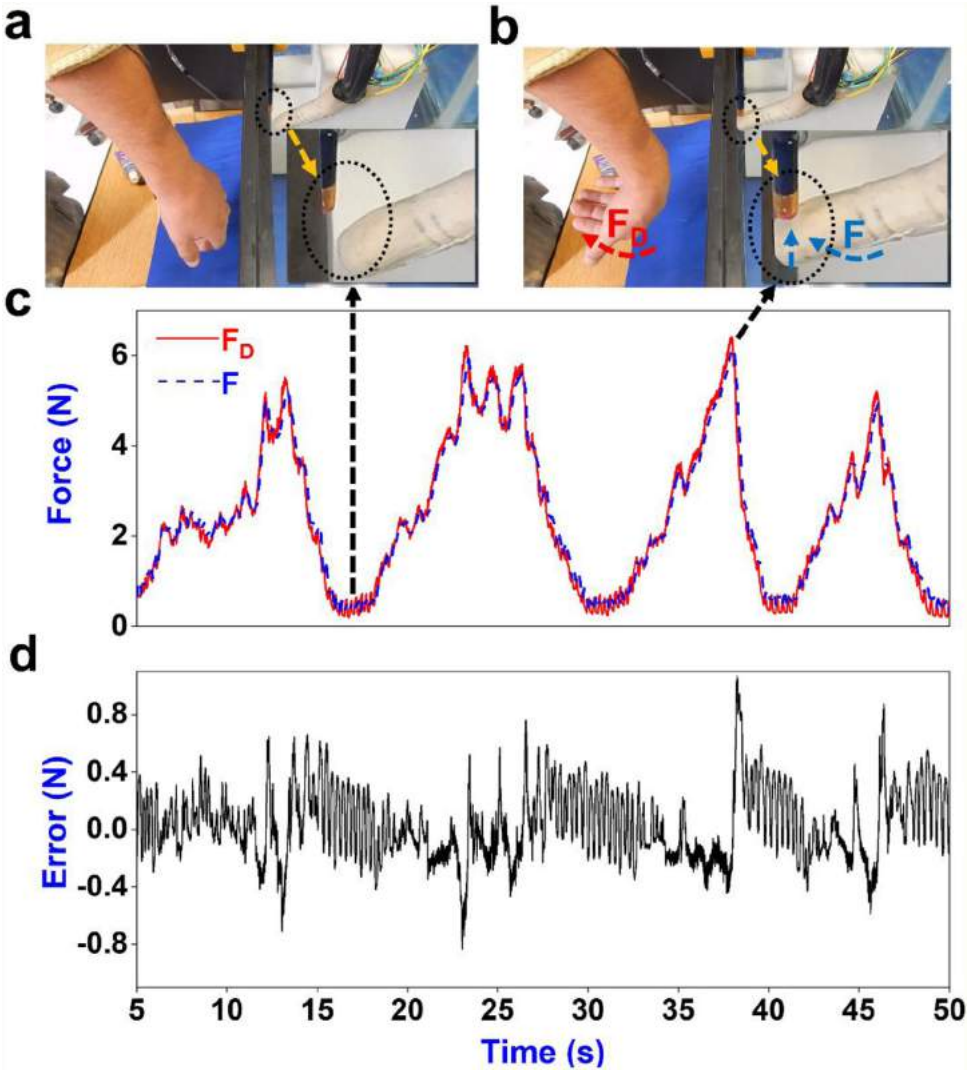

Fig. 7. EMG input to control the fingertip force. a. When the forearm muscles were relaxed, the desired force was nearly zero and the finger was not contacting the pencil. b. As the wrist flexor muscle contracted, the desired force increased and the SMA finger responded by matching the desired force on each cycle of flexion and extension. c. The force tracking responses of the SMA actuated finger consistently tracked the desired force specified by the EMG signals. d. The force tracking error was always less than 1 N and the mean absolute error was 0.32 N.

impacted the mean absolute error over this range of operational conditions ($p > 0.05$).

3.3. Electromyogram control of the submerged robotic finger

A person was able to capably control the desired force using EMG as the input to the nonlinear controller. When the person's forearm muscles were relaxed, the desired force was near zero, and the finger was not contacting the pencil (Fig. 7a). As the wrist flexor muscle was contracted (Fig. 7b), the desired force increased and the SMA finger responded by matching the desired force (Fig. 7c). As the person repeatedly flexed and extended his wrist, the soft robotic finger responded by flexing and extending, reliably tracking the EMG input signal. The force tracking error of the SMA actuated finger during this demonstration never exceeded 1 N and the mean absolute error was 0.32 N (Fig. 7c). Video of the EMG control experiment was recorded and shown in supplemental video 3.

3.4. Finite element results

A comparison between the experimental and simulated motions of the flexor actuator showed that Joule heating the SMA caused the actuator to flex; the displacement increased for approximately 1 s, and then it relaxed slightly (Fig. 8). The absolute mean error between the simulated and experimental displacement was

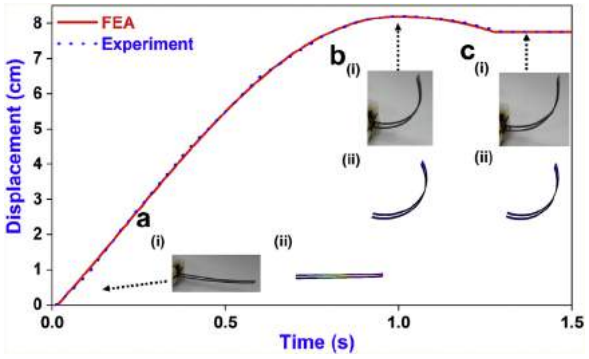

Fig. 8. The experimental and simulated motions of the flexor actuator showed that Joule heating the SMA caused the finger to flex. a (i) The actual SMA shape. (ii) The simulated displacement field at the initial stage. b (i) The actual SMA shape. (ii) The simulated displacement field at 1 s. c (i) The actual SMA shape. (ii) The simulated displacement field at the last stage.

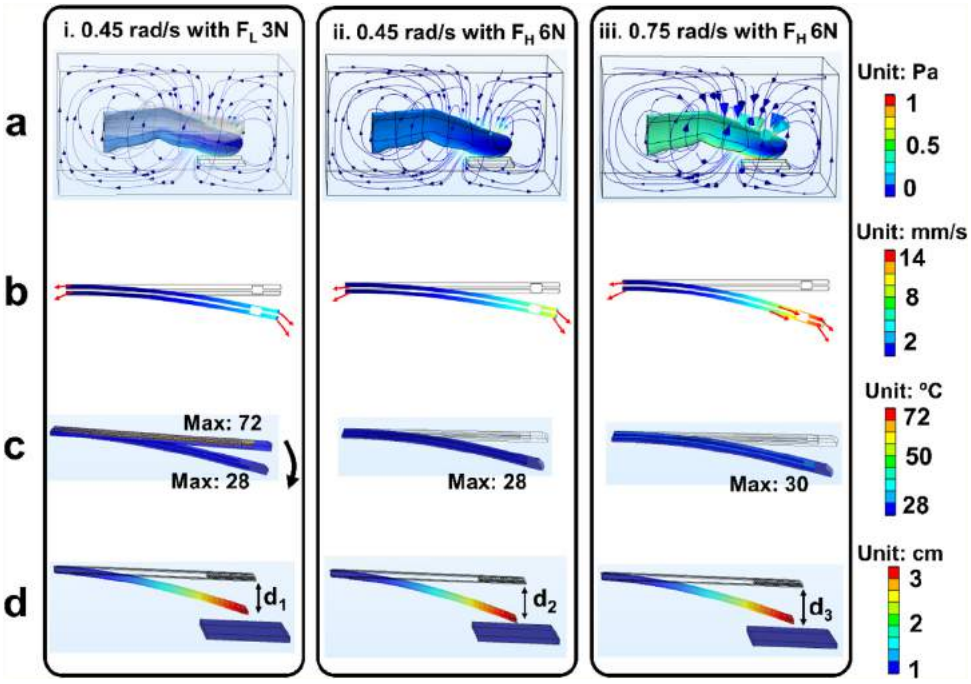

Fig. 9. Thermal-fluidic-structural system of an underwater manipulator. a. The fluid field of the environmental water in which larger arrows indicate higher velocity. The pressure of the fluid on the finger surface showed an increasing trend with increasing input force amplitude and frequency. b. The velocity field of the SMA inside the water. c. The thermal field of SMA in which red means a higher temperature, blue means a lower temperature. d. The displacement field of the sensor in which red means a higher displacement, blue means a lower displacement. All conditions a-d were under (i) 0.45 rad/s with low (F_L) amplitude desired force input of 3 N (ii) 0.45 rad/s with high (F_H) amplitude desired force input of 6 N (iii) 0.75 rad/s with high (F_H) amplitude desired force input of 6 N.

0.048 cm. The experimental video and simulation video were compared and shown in Supplemental Video 1.

Fig. 9a shows the fluid and pressure fields underwater in which larger arrows indicate higher velocities of the environmental fluid flow. The velocity and pressure changed slightly under the two different amplitudes (Fig. 9a (i–ii)), while the overall velocity and the pressure on the finger's external surface increased more substantially with the higher frequency (Fig. 9a (ii–iii)). The finger generated viscous drag force in the environmental fluid, while the system was stable under both frequencies and amplitudes.

Fig. 9b shows the velocity fields of the internal water surrounding the SMA actuators within the finger. The results showed that the water flowed outward from two sides of the SMA actuator cavities as the actuator flexed, and the velocity increased from 3 mm/s under the low force amplitude condition (Fig. 9b(i)) to 5 mm/s under the high amplitude condition (Fig. 9b(ii)), which yielded a larger fingertip displacement (d_2, Fig. 9d(ii)) compared to the low amplitude case (d_1, Fig. 9d(i)). Then, the exit velocity of the fluid within the SMA actuators increased from 5 mm/s to 12 mm/s with the 0.75 rad/s frequency (Fig. 9b (iii), which produced a smaller actuator displacement (d_3, Fig. 9d(iii)). This interesting observation is consistent with experimental results, where the sinusoidal tracking error increased with the highest frequency and amplitude experiment (Fig. 6(b)).

Fig. 9c shows the thermal field of SMA in which red means a higher temperature, blue means a lower temperature. The results showed that the red region had a maximum temperature of about 72 °C and then it cooled down to 28 °C with the 0.45 rad/s frequency (Fig. 9c (i)). The same trend could be seen in Fig. 9c (ii). However, there were some areas around 30 °C with the 0.75 rad/s frequency (Fig. 9c (iii)), which indicated that the phase transition of the SMA was not fully completed (Table 1). This also correlates to the larger tracking error observed with the high frequency and high amplitude tracking experiments (Fig. 6(b)).

Fig. 9d shows the displacement field of the sensors in which red means a higher displacement, blue means a lower displacement. The results showed that the displacement (d_1) was smaller than the high amplitude/low frequency simulation (d_2) so the distance between the sensor and the object with the low amplitude force input was higher (Fig. 9d (i–ii)). With the high amplitude/high frequency of 0.75 rad/s, the displacement (d_3, Fig. 9d (iii)) was lower than that with 0.45 rad/s (d_2, Fig. 9d(ii)). This is corroborated experimentally by the larger mean force tracking error that was observed in the high frequency/high amplitude cycles in comparison to the other conditions that were tested (Fig. 6b). Because the exit velocity of the water surrounding the SMA actuators was faster with the high frequency/amplitude sine input, there was less water mass available within the finger to rapidly cool the flexor actuator after the heating cycle. This produced an incomplete phase transition of the SMA material, resulting in smaller deformation and corresponding lower applied force, producing larger tracking error in the experimental results (Fig. 6b).

4. Discussion

In this study, we developed a multi-layered tactile sensor on the housing for the SMA plates that were trained to take a curved shape to achieve force control of the underwater robotic finger. Results showed that the soft robotic finger has promising potential to precisely manipulate delicate submerged objects using feedback from the compliant, multi-layered tactile sensor through the newly developed nonlinear force control system. The step and sinusoidal experiments showed satisfactory force tracking ability, and the action of the nonlinear force feedback controller rapidly minimized the error.

Some prior techniques have been developed to assemble sensors onto underwater manipulator systems [47,48]. Although assembled sensors could provide force feedback for the manipulator systems, the procedures include multiple steps to assemble the

sensor in the system and waterproofing sensors is a challenge. The method to directly print the stretchable sensor onto the SMA actuator mold in this paper is a much simpler technique as it can be accurately designed by 3D modeling and directly 3D-printed as part of a reliable and repeatable manufacturing process. The embedded sensor was sufficiently robust, waterproof, and the printing procedure could be much cheaper than traditional methods involving multiple assembly steps. In these aspects, the embedded force sensor design and printing process presented in this paper has a significant advantage.

Additionally, the nonlinear controller, which enables precise fingertip force control using feedback from the compliant tactile sensor, could be used to grasp delicate objects underwater, and the finger itself has high compliance inherently due to the soft and flexible manufacturing process [49,50]. This grasping device not only acts as a soft gripper but also provides real-time force feedback control to prevent inadvertent damage.

In this study, the EMG control system for the underwater manipulator has also shown proof of concept for a new method to proportionally control the grip force of a submerged manipulator by adapting an intuitive biosignal processing technique from biomedical applications into the underwater domain [51–53]. This has provided a new option for people to remotely control the grip force of underwater manipulators, which has not been previously published, to the best knowledge of the authors. Furthermore, this novel finger could be scaled up in the future to create a dexterous multi-digit hand manipulator [54] for more complex tasks and could be coupled with sophisticated EMG pattern recognition algorithms for dexterous control capabilities [55].

New in this paper was also the development of a 3D finite element mathematic model considering the thermal-fluidic-structural multi-physics behavior of the manipulator underwater. It not only verified the shape memory behavior of the SMA actuator, but also provided an explanation for the interaction between the cooling rate and Joule heating of the flexor and extensor SMA actuators underwater. It is still challenging to design soft gripping manipulators that undergo active deformations; hence this new modeling approach could be useful for guiding the design of new underwater manipulators with different material properties deployed in diverse environments and control situations. To take all the factors into account, the dynamical performances of the soft manipulators with arbitrary geometries as well as the active control schemes need to be determined jointly with the induced fluidic motions. For example, the higher environmental fluidic velocities produced by the high-amplitude finger motions (Fig. 9 a(iii)) could induce more disturbance of silt compared to the low amplitude finger motions (Fig. 9 a(i)), which can visually occlude the grasp site and impede tele-operated control of the manipulator. To enable a multidisciplinary understanding of improved gripping mechanisms, a blend of experimental studies coupled with accurate modeling and simulations in design, fabrication, analysis, and optimization is needed. The scale of the design space for soft robotic manipulators with integrated stretchable sensors, particularly for underwater applications, is truly daunting. The newly developed 3D model for this actuator could help guide future innovations in this challenging field.

5. Conclusion

An SMA-driven anthropomorphic underwater robotic finger has been designed and manufactured with an embedded tactile sensor that was directly 3D-printed within a hybrid manufacturing process. The embedded sensor was sufficiently robust, and the printing procedure could be much cheaper than traditional methods involving multiple assembly steps. The nonlinear force controller worked successfully using tactile feedback from the stretchable sensor to rapidly minimize tracking error and provide stable grasp performance. Based on the closed-loop feedback from the directly 3D-printed tactile sensor, both step and sinusoidal tracking experiments demonstrated satisfactory error minimization while the novel finger was actuated underwater. Additionally, a person was readily capable of controlling the desired force with high accuracy using EMG signals. The thermal-fluidic-structural multi-physics behavior of the manipulator underwater was explained by a 3D finite element model, which not only verified the shape memory behavior of both actuators, but also provided a new method to understand the interaction between the cooling rate and Joule heating of shape memory actuators underwater. In summary, the novel manipulator system with the directly 3D-printed tactile sensor has promising potential to delicately grasp fragile objects underwater.

Authorship statement

All persons who meet authorship criteria are listed as authors, and all authors certify that they have participated sufficiently in the work to take public responsibility for the content, including participation in the concept, design, analysis, writing, or revision of the manuscript. Furthermore, each author certifies that this material or similar material has not been and will not be submitted to or published in any other publication before its appearance in the *Sensors and Actuators A: Physical.*

Authorship contributions

Please indicate the specific contributions made by each author (list the authors' initials followed by their surnames, e.g., Y.L. Cheung). The name of each author must appear at least once in each of the three categories below.

Category 1

Conception and design of study: M.H. Lin, E.D. Engeberg, S. Dilibal, J. Choi, M. Vatani;

acquisition of data: M.H. Lin, E.D. Engeberg;

analysis and/or interpretation of data: M.H. Lin, E.D. Engeberg.

Category 2

Drafting the manuscript: M.H. Lin, M. Vatani, E.D. Engeberg, J. Choi, S. Dilibal;

revising the manuscript critically for important intellectual content: M.H. Lin, E.D. Engeberg, J. Choi, S. Dilibal.

Category 3

Approval of the version of the manuscript to be published (the names of all authors must be listed):

M.H. Lin, M. Vatani, J.W. Choi, S. Dilibal, E.D. Engeberg.

Declaration of Competing Interest

The authors report no declarations of interest.

Acknowledgments

This research was supported in part by NIH1R01EB025819 and NSF awards 1317952, 1536136, 1265145, and 1659484, and by the Department of Energy contract TOA#0000403076. The authors

would like to thank Mr. D. Dieujuste for help to create video supplements and images. The authors would also like to thank Dr. K. Mondal for his assistance with editing the manuscript.

Appendix A. Supplementary data

Supplementary material related to this article can be found, in the online version, at doi:https://doi.org/10.1016/j.sna.2020.112221.

References

[1] A. Aggarwal, P. Kampmann, J. Lemburg, F. Kirchner, Haptic object recognition in underwater and deep-sea environments, J. Field Robot. 32 (2015) 167–185.
[2] Q. Meng, H. Wang, P. Li, L. Wang, Z. He, Dexterous underwater robot hand: HEU hand II, in: 2006 International Conference on Mechatronics and Automation, IEEE, 2006, pp. 1477–1482.
[3] H.S. Stuart, M. Bagheri, S. Wang, H. Barnard, A.L. Sheng, M. Jenkins, et al., Suction helps in a pinch: improving underwater manipulation with gentle suction flow, in: 2015 IEEE/RSJ International Conference on Intelligent Robots and Systems (IROS), IEEE, 2015, pp. 2279–2284.
[4] R.S. Dahiya, G. Metta, M. Valle, G. Sandini, Tactile sensing—from humans to humanoids, IEEE Trans. Robot. 26 (2009) 1–20.
[5] J. Dennerlein, R. Howe, E. Shahoian, C. Olroyd, Vibrotactile feedback for an underwater telerobot, robotics and applications, in: Robotic and manufacturing systems recent results in research, development and applications International symposium, 8th, Citeseer, 2000, pp. 244–249.
[6] Z. Shen, H. Zhong, E. Xu, R. Zhang, K.C. Yip, L.L. Chan, et al., An underwater robotic manipulator with soft bladders and compact depth-independent actuation, Soft Robot. (2020).
[7] H. Yousef, M. Boukallel, K. Althoefer, Tactile sensing for dexterous in-hand manipulation in robotics—a review, Sens. Actuators A Phys. 167 (2011) 171–187.
[8] M.I. Tiwana, S.J. Redmond, N.H. Lovell, A review of tactile sensing technologies with applications in biomedical engineering, Sens. Actuators A Phys. 179 (2012) 17–31.
[9] X. Liao, W. Wang, M. Lin, M. Li, H. Wu, Y. Zheng, Hierarchically distributed microstructure design of haptic sensors for personalized fingertip mechanosensational manipulation, Mater. Horiz. 5 (2018) 920–931.
[10] D.M. Lane, J.B.C. Davies, G. Robinson, D.J. O'Brien, J. Sneddon, E. Seaton, et al., The AMADEUS dextrous subsea hand: design, modeling, and sensor processing, IEEE J. Ocean. Eng. 24 (1999) 96–111.
[11] K.C. Galloway, K.P. Becker, B. Phillips, J. Kirby, S. Licht, D. Tchernov, et al., Soft robotic grippers for biological sampling on deep reefs, Soft Robot. 3 (2016) 23–33.
[12] D.M. Vogt, K.P. Becker, B.T. Phillips, M.A. Graule, R.D. Rotjan, T.M. Shank, et al., Shipboard design and fabrication of custom 3D-printed soft robotic manipulators for the investigation of delicate deep-sea organisms, PLoS One 13 (2018), e0200386.
[13] N.R. Sinatra, C.B. Teeple, D.M. Vogt, K.K. Parker, D.F. Gruber, R.J. Wood, Ultragentle manipulation of delicate structures using a soft robotic gripper, Sci. Robot. 4 (2019).
[14] P. Ahuja, S. Akiyama, S.K. Ujjain, R. Kukobat, F. Vallejos-Burgos, R. Futamura, et al., A water-resilient carbon nanotube based strain sensor for monitoring structural integrity, J. Mater. Chem. A 7 (2019) 19996–20005.
[15] J. Wu, Z. Li, X. Xie, K. Tao, C. Liu, K.A. Khor, et al., 3D superhydrophobic reduced graphene oxide for activated NO 2 sensing with enhanced immunity to humidity, J. Mater. Chem. A 6 (2018) 478–488.
[16] R. Xu, K. Zhang, X. Xu, M. He, F. Lu, B. Su, Superhydrophobic WS2-nanosheet-wrapped sponges for underwater detection of tiny vibration, Adv. Sci. 5 (2018), 1700655.
[17] Y.F. Zhang, Y.W. Liu, M.H. Jin, H. Liu, Design of a finger-tip flexible tactile sensor for an anthropomorphic robot hand, International Conference on Intelligent Robotics and Applications (2010) 762–773, Springer.
[18] F.L. Hammond, R.K. Kramer, Q. Wan, R.D. Howe, R.J. Wood, Soft tactile sensor arrays for micromanipulation, in: 2012 IEEE/RSJ International Conference on Intelligent Robots and Systems, IEEE, 2012, pp. 25–32.
[19] M. Vatani, M. Vatani, J. Choi, Multi-layer stretchable pressure sensors using ionic liquids and carbon nanotubes, Appl. Phys. Lett. 108 (2016), 061908.
[20] J. Lee, M.O.F. Emon, M. Vatani, J.W. Choi, Effect of degree of crosslinking and polymerization of 3D printable polymer/ionic liquid composites on performance of stretchable piezoresistive sensors, Smart Mater. Struct. 26 (2017), 035043.
[21] I. Kang, M.J. Schulz, J.H. Kim, V. Shanov, D. Shi, A carbon nanotube strain sensor for structural health monitoring, Smart Mater. Struct. 15 (2006) 737.
[22] M. Shokrieh, R. Rafiee, A review of the mechanical properties of isolated carbon nanotubes and carbon nanotube composites, Mech. Compos. Mater. 46 (2010) 155–172.
[23] N. Hu, Z. Masuda, C. Yan, G. Yamamoto, H. Fukunaga, T. Hashida, The electrical properties of polymer nanocomposites with carbon nanotube fillers, Nanotechnology 19 (2008), 215701.
[24] N. Hu, H. Fukunaga, S. Atobe, Y. Liu, J. Li, Piezoresistive strain sensors made from carbon nanotubes based polymer nanocomposites, Sensors 11 (2011) 10691–10723.
[25] C. Liu, Recent developments in polymer MEMS, Adv. Mater. 19 (2007) 3783–3790.
[26] M. Park, H. Kim, J.P. Youngblood, Strain-dependent electrical resistance of multi-walled carbon nanotube/polymer composite films, Nanotechnology 19 (2008), 055705.
[27] T. Sekitani, Y. Noguchi, K. Hata, T. Fukushima, T. Aida, T. Someya, A rubberlike stretchable active matrix using elastic conductors, Science 321 (2008) 1468–1472.
[28] Y.Y. Huang, E.M. Terentjev, Tailoring the electrical properties of carbon nanotube–polymer composites, Adv. Funct. Mater. 20 (2010) 4062–4068.
[29] K.Y. Chun, Y. Oh, J. Rho, J.H. Ahn, Y.J. Kim, H.R. Choi, et al., Highly conductive, printable and stretchable composite films of carbon nanotubes and silver, Nat. Nanotechnol. 5 (2010) 853.
[30] R. Ma, S. Kwon, Q. Zheng, H.Y. Kwon, J.I. Kim, H.R. Choi, et al., Carbon-nanotube/silver networks in nitrile butadiene rubber for highly conductive flexible adhesives, Adv. Mater. 24 (2012) 3344–3349.
[31] E.D. Engeberg, S. Dilibal, M. Vatani, J.W. Choi, J. Lavery, Anthropomorphic finger antagonistically actuated by SMA plates, Bioinspir. Biomim. 10 (2015), 056002.
[32] B.A. Kent, N. Karnati, E.D. Engeberg, Electromyogram synergy control of a dexterous artificial hand to unscrew and screw objects, J. Neuroeng. Rehabil. 11 (2014) 41.
[33] S. Dilibal, Stabilized actuation of a novel niti shape-memory-alloy-actuated flexible structure under thermal loading, Mater. Tehnol. 52 (2018) 599–605.
[34] M. Vatani, E.D. Engeberg, J.W. Choi, Force and slip detection with direct-write compliant tactile sensors using multi-walled carbon nanotube/polymer composites, Sens. Actuators A Phys. 195 (2013) 90–97.
[35] M. Emon, J.W. Choi, Flexible piezoresistive sensors embedded in 3D printed tires, Sensors 17 (2017) 656.
[36] D. Hughes, N. Correll, Texture recognition and localization in amorphous robotic skin, Bioinspir. Biomim. 10 (2015), 055002.
[37] C. Cipriani, F. Zaccone, S. Micera, M.C. Carrozza, On the shared control of an EMG-controlled prosthetic hand: analysis of user–prosthesis interaction, IEEE Trans. Robot. 24 (2008) 170–184.
[38] L. Lucas, M. DiCicco, Y. Matsuoka, An EMG-controlled hand exoskeleton for natural pinching, J. Robot. Mechatron. 16 (2004) 482–488.
[39] J. Arghavani, F. Auricchio, R. Naghdabadi, A finite strain kinematic hardening constitutive model based on Hencky strain: general framework, solution algorithm and application to shape memory alloys, Int. J. Plast. 27 (2011) 940–961.
[40] D.C. Lagoudas, Z. Bo, M.A. Qidwai, A unified thermodynamic constitutive model for SMA and finite element analysis of active metal matrix composites, Mech. Compos. Mater. Struct. 3 (1996) 153–179.
[41] S. Akbari, A.H. Sakhaei, S. Panjwani, K. Kowsari, A. Serjourei, Q. Ge, Multimaterial 3D printed soft actuators powered by shape memory alloy wires, Sens. Actuators A Phys. 290 (2019) 177–189.
[42] L. Petrini, F. Migliavacca, P. Massarotti, S. Schievano, G. Dubini, F. Auricchio, Computational Studies of Shape Memory Alloy Behavior in Biomedical Applications, 2005.
[43] H. Fang, S. Wang, L. Zhou, N. Zhou, M. Lin, Influence of furnace design on the thermal stress during directional solidification of multicrystalline silicon, J. Cryst. Growth 346 (2012) 5–11.
[44] F. Gao, H. Ueda, L. Gang, H. Okada, Fluid structure interaction simulation in three-layered aortic aneurysm model under pulsatile flow: comparison of wrapping and stenting, J. Biomech. 46 (2013) 1335–1342.
[45] X. Wang, M. Lin, Y. Kang, Engineering porous β-Tricalcium phosphate (β-TCP) scaffolds with multiple channels to promote cell migration, proliferation, and angiogenesis, ACS Appl. Mater. Interfaces 11 (2019) 9223–9232.
[46] M. Lin, N. Firoozi, C.T. Tsai, M.B. Wallace, Y. Kang, 3D-printed flexible polymer stents for potential applications in inoperable esophageal malignancies, Acta Biomater. 83 (2019) 119–129.
[47] P. Kampmann, F. Kirchner, Towards a fine-manipulation system with tactile feedback for deep-sea environments, Rob. Auton. Syst. 67 (2015) 115–121.
[48] G.G. Muscolo, G. Cannata, A Novel Tactile Sensor for Underwater Applications: Limits and Perspectives, OCEANS 2015-Genova, IEEE, 2015, pp. 1–7.
[49] C. Gambini, B. Abou, A. Ponton, A.J. Cornelissen, Micro-and macrorheology of jellyfish extracellular matrix, Biophys. J. 102 (2012) 1–9.
[50] M.J. Abrams, T. Basinger, W. Yuan, C.L. Guo, L. Goentoro, Self-repairing symmetry in jellyfish through mechanically driven reorganization, Proc. Natl. Acad. Sci. 112 (2015) E3365–E3373.
[51] A. Fougner, Ø. Stavdahl, P.J. Kyberd, Y.G. Losier, P.A. Parker, Control of upper limb prostheses: terminology and proportional myoelectric control—a review, IEEE Trans. Neural Syst. Rehabil. Eng. 20 (2012) 663–677.
[52] M.A. Oskoei, H. Hu, Myoelectric control systems—a survey, Biomed. Signal Process. Control 2 (2007) 275–294.
[53] P. Geethanjali, Myoelectric control of prosthetic hands: state-of-the-art review, Med. Dev. (Auckland, NZ) 9 (2016) 247.
[54] B.A. Kent, E.D. Engeberg, Robotic hand acceleration feedback to synergistically prevent grasped object slip, IEEE Trans. Robot. 33 (2016) 492–499.
[55] A.H. Al-Timemy, G. Bugmann, J. Escudero, N. Outram, Classification of finger movements for the dexterous hand prosthesis control with surface electromyography, IEEE J. Biomed. Health Inform. 17 (2013) 608–618.

Biographies

Dr. Lin received his B.S. and M.S. in material science and technology from Fuzhou University and Nanchang University, respectively, and the Ph.D. degree in mechanical engineering from Florida Atlantic University. He is currently a research scientist in the Department of Ocean & Mechanical Engineering at Florida Atlantic University. His research interests include sensor design, soft robotics, medical device, 3D printing, simulation and modeling. His studies have resulted in several awards and over 30 journal articles and conference papers.

Dr. Vatani received B.S., M.S., and Ph.D. degrees in the mechanical engineering department from Isfahan University of Technology, Amir Kabir University of Technology, and University of Akron, respectively. His main research area was on additive manufacturing of stretchable tactile sensors, Processes, Materials, and Applications. In various capacities, He has worked on additive manufacturing for the past decade, leading the development of novel materials, hardware, and processes for additive manufacturing of active objects ranging from biomedical engineering to energy storage devices. His studies resulted in several awards, patents, and over 40 journal articles, conference papers, and talks internationally.

Dr. Choi received the B.S., M.S. and Ph.D. degrees in the mechanical engineering department from Pusan National University, Busan, Korea, in 1999, 2001, and 2007, respectively. He is now an Associate Professor in the department of mechanical engineering at University of Akron. His research interests include development of additive manufacturing processes and materials, with applications of 3D printed smart structures (sensors, actuators and electronics), 3D printed rubbers for insoles and tires, biofabrication and hybrid processes for metals/ceramics. He is currently serving as an associate editor in Additive Manufacturing; editorial member in International Journal of Precision Engineering and Manufacturing – Green Technology.

Dr. Dilibal received his BS in System Engineering from Army Academy, M.Sc. in Mechanical Engineering from Istanbul Technical University, and his Ph.D. in Materials Engineering from Yildiz Technical University. He has a strong background in processing-microstructure-property relationships of SMAs. He completed a postdoctoral fellowship at the University of Illinois at Urbana-Champaign. He was an adjunct faculty in the Mechanical Engineering Department at the University of Akron. He worked in a NASA-funded, SMA-related project. He is the head of Mechatronics Engineering Department at Istanbul Gedik University as an associate professor. He is the director of the Robot Technology Research, Application Center.

Dr. Engeberg received his B.S. and Ph.D. in Mechanical Engineering from Walla Walla University in 2003 and the University of Utah in 2008, respectively. He is now an Associate Professor in the Department of Ocean & Mechanical Engineering at Florida Atlantic University. His research interests include bioinspired and biomedical robotics, sensors, actuators, and control. He has been awarded 8 patents and has published over 80 peer reviewed journal and conference papers. He often serves as the Associate Editor of robotics conferences including the IEEE International Conference on Robotics and Automation.